

Stability and characteristic modes of skyrmions in magnetic nanotubes

Tijjani Abdulrazak, Qizhi Cai(蔡淇智), and Guangwei Deng(邓光伟)
Citation: Chin. Phys. B, 2025, 34 (**10**): 107512. DOI: 10.1088/1674-1056/ade071
http://cpb.iphy.ac.cn; http://iopscience.iop.org/cpb

What follows is a list of articles you may be interested in

Effect of interlayer interaction on magnon properties of vdW honeycomb heterostructures

Jun Shan(单俊), Lichuan Zhang(张礼川), Huasu Fu(付华宿), Yuee Xie(谢月娥), Yuriy Mokrousov, and Yuanping Chen(陈元平)
Chin. Phys. B, 2025, 34 (**8**): 087501. DOI: 10.1088/1674-1056/adce97

Deformation of magnetic skyrmion due to skyrmion-skyrmion interaction

Zhen-Qian Cui(崔振茜), Wen-Li Yang(杨文力), and Jun-Hui Zheng(郑俊辉)
Chin. Phys. B, 2025, 34 (**7**): 077502. DOI: 10.1088/1674-1056/adca20

First- and second-order magnonic topologies in the ferromagnetic breathing SSH model modulated by non-Hermitian effects

Huasu Fu(付华宿), Lichuan Zhang(张礼川), Rami Mrad, Yuee Xie(谢月娥), and Yuanping Chen(陈元平)
Chin. Phys. B, 2025, 34 (**6**): 067506. DOI: 10.1088/1674-1056/addaa0

Multiferroicity and thermal expansion of the layered metal-organic framework $[NH_4Cl]_2[Ni(HCOO)_2(NH_3)_2]$

Dan Cheng(程丹), Yingjie He(何英杰), Shuang Liu(刘爽), Na Su(苏娜), and Young Sun(孙阳)
Chin. Phys. B, 2025, 34 (**6**): 067505. DOI: 10.1088/1674-1056/adcaa4

Influence of cooling atmosphere on the structure, magnetization, and dielectric properties of $CaBaCo_4O_7$

Gaoshang Gong(龚高尚), Minghao Wang(王明豪), Ruoshui Liu(刘若水), Yang Wu(吴杨), Lichen Wang(王利晨), Yongqiang Wang(王永强), and Baogen Shen(沈保根)
Chin. Phys. B, 2025, 34 (**4**): 047502. DOI: 10.1088/1674-1056/adbadc

---

Stability and characteristic modes of skyrmions in magnetic nanotubes

Tijjani Abdulrazak[1,2,†], Qizhi Cai(蔡淇智)[1,3], and Guangwei Deng(邓光伟)[1,3,4,‡]

[1] *Institute of Fundamental and Frontier Sciences, University of Electronic Science and Technology of China, Chengdu* 611731, *China*
[2] *Department of Physics, Bayero University, Kano* 700006, *Nigeria*
[3] *Key Laboratory Quantum Physics and Photonic Quantum Information, Ministry of Education, University of Electronic Science and Technology of China, Chengdu* 610054, *China*
[4] *Institute of Electronics and Information Industry Technology of Kash, Kash* 844000, *China*

(Received 17 April 2025; revised manuscript received 30 May 2025; accepted manuscript online 4 June 2025)

We study the stability and dynamic behaviors of skyrmions in magnetic nanotubes, where curvature and cylindrical symmetry provide unique mechanisms for skyrmion formation and control. Unlike planar geometries, skyrmions confined in nanotubes exhibit elliptical shapes, stabilized through the interplay of curvature-induced effects, Dzyaloshinskii–Moriya interaction (DMI), and magnetic anisotropy. Using micromagnetic simulations, we construct phase diagrams of skyrmion stability as functions of DMI strength and anisotropy, identifying transitions to saturated or helical configurations in unstable regimes. The dynamics reveal distinct counterclockwise gyration modes, strongly influenced by tube geometry and applied microwave fields. We find that external magnetic fields significantly enhance the azimuthal velocity ($\bar{v}_\phi$) while maintaining a consistent axial motion ($\bar{v}_z$) along the $-z$-direction. Furthermore, transitions between gyration and linear translation modes emerge, governed by the combined effects of magnetic field, DMI, and curvature. Notably, the skyrmion's motion direction depends on the excitation mode and DMI sign, while curvature-modified spin textures produce effective fields without conventional pinning. These results demonstrate that magnetic nanotubes offer a robust and tunable platform for skyrmion manipulation, with potential applications in next-generation memory and logic devices. Our findings also highlight the role of curvature in enabling stable and controllable topological spin textures for advanced spintronic technologies.

Keywords: ferromagnetic, magnetic field, MuMax3 software, skyrmion, spin wave

PACS: 75.50.Gg, 71.35.Ji, 12.39.Dc, 75.30.Ds

DOI: 10.1088/1674-1056/ade071 **CSTR:** 32038.14.CPB.ade071

1. Introduction

Magnetic skyrmions are topologically protected spin textures with particle-like properties. They have garnered significant attention for their potential in spintronic applications, such as magnetic memory devices, neuromorphic computing, and logic circuits.[1–6] Their nanoscale dimensions, low energy consumption, and robust stability make them ideal for next-generation information technologies, since reliable control of skyrmion motion is essential for such applications.[1,7–13] While early work demonstrated that small spin-transfer torques could mobilize skyrmion lattices,[8,9] achieving long-distance, stable transport of isolated skyrmions remains a major challenge in real-world systems. In planar geometries, the skyrmion Hall effect causes lateral drift toward device edges, often resulting in annihilation and data loss.[2,15,16] The Dzyaloshinskii–Moriya interaction (DMI), arising from spin–orbit coupling in noncentrosymmetric environments, plays a key role in stabilizing skyrmions.[17,18] Two main types of DMI are recognized: intrinsic bulk DMI, which stabilizes Bloch-type skyrmions in materials like MnSi and FeGe,[19–21] and interfacial DMI, responsible for Néel-type skyrmions in layered structures such as Ir(111)/Fe and [Ir/Co/Pt] multilayers.[7,22] Advancements in microstructural technology have enabled the creation of three-dimensional (3D) magnetic structures with complex geometries and varying sizes, using a variety of chemical and physical processes. Among the different geometric forms of magnetic objects, magnetic nanotubes offer unique geometrical characteristics, such as length, inner radius, thickness, and outer radius, allowing designers to manipulate their designs' magnetic properties. Theoretical and experimental studies have both demonstrated that curvature can significantly impact magnetic textures,[23–30] influencing their stability, mobility, and mode excitation.[31–43] The edge-free azimuthal boundary and curvature-modified demagnetizing field further reduce the restoring force on the skyrmion, resulting in red-shifted resonance frequencies and potential mode hybridization.[34] Previous research with micromagnetic simulations has unveiled the dynamic and static characteristics of Bloch skyrmions in magnetic cylindrical nanotubes. Wang *et al.*[44] demonstrated that skyrmions can move along the tube surface without annihilating, even at high current densities. Huo *et al.*[6] discovered

†Corresponding author. E-mail: atijjani.phy@buk.edu.ng
‡Corresponding author. E-mail: gwdeng@uestc.edu.cn

© 2025 Chinese Physical Society and IOP Publishing Ltd. All rights, including for text and data mining, AI training, and similar technologies, are reserved.

that elliptical skyrmions can exist in nanotubes over a range of magnetic fields. Furthermore, Yang *et al.*[45] found that the stability of skyrmions in an elliptical form is influenced by the sign of the DMI constant, with curved geometry playing an important role. The dynamic modes of skyrmions in these magnetic nanotubes include two in-plane gyration modes, rotating clockwise (CW) and counterclockwise (CCW), as well as one out-of-plane breathing mode.

Recent works have underscored the role of geometry and curvature in stabilizing and manipulating skyrmions in curved nanostructures. Ga *et al.*[46] have shown that geometric curvature alone can induce substantial DMI and stabilize skyrmions in low-dimensional magnetic materials. Using first-principles calculations and spin simulations, they demonstrated that curvature-induced inversion symmetry breaking in a model 1D nanoribbon of $CrBr_2$ and a 2D $MnSe_2$ monolayer leads to tunable DMI and enables field-free skyrmion formation. Their findings highlight curvature as a powerful design strategy for engineering chiral spin textures in flexible and low-dimensional spintronic devices. Similarly, Jiang *et al.*[47] introduced the concept of origami-driven DMI in centrosymmetric 2D magnets, showing how spin–orbit coupling and geometric folding can generate Néel-type DMI and chiral domain walls in folded CrI_3 systems. Although these studies revealed foundational insights into curvature-induced effects and topological spin textures, they did not address dynamic mode excitations or frequency-resolved behavior.

In this work, we study the stability of single skyrmions in magnetic curved nanostructures and their characteristic modes when subjected to a spin-wave magnetic field. Specifically, we examine skyrmions in magnetic nanotubes as a function of magnetic and geometrical properties. This research primarily addresses the DMI and anisotropy constant as key factors in skyrmion stability, although dipole interactions and frustration interactions can also play important roles in certain contexts. In particular, dipole interactions may contribute to stabilization in systems with significant magnetic moments,[48,49] and frustration interactions can induce non-collinear spin arrangements, which may also support skyrmionic structures.[50–52] We identify distinct gyration modes and analyze how curvature modifies the direction and character of skyrmion motion. Our results reveal mode-dependent translational behavior, elliptical deformation, and transitions to helical states as a function of material and geometric parameters.

2. Model and methods

We consider a system composed of hollow cylinder magnetic nanotubes with length $L = 600$ nm, varying wall thickness $d = 10$–40 nm, inner radius $r = 30$ nm, and outer radius $R = 50$ nm. A schematic of the nanotube and its cylindrical coordinate system-defined by $\hat{\rho}$, $\hat{\phi}$, and $\hat{z}$ directions is presented in Fig. 1, with the origin located at the center of the tube. We performed micromagnetic simulations using GPU-accelerated MuMax3 software,[53] which numerically solves the Landau–Lifshitz–Gilbert (LLG) equation

$$\frac{\partial \boldsymbol{m}}{\partial t} = -\gamma \boldsymbol{m} \times \boldsymbol{H}_{\text{eff}} + \alpha \boldsymbol{m} \times \frac{\partial \boldsymbol{m}}{\partial t}, \tag{1}$$

where γ is the gyromagnetic ratio, $\boldsymbol{m}$ is the normalized magnetization vector, α is the Gilbert damping constant, and $\boldsymbol{H}_{\text{eff}} = -M_{\text{s}}^{-1}\delta\varepsilon/\delta\boldsymbol{m}$ represents the effective magnetic field. The total magnetic energy density ε includes the contributions from exchange interaction ε_{ex}, bulk DMI ε_{DMI}, uniaxial anisotropy ε_K, and dipole–dipole interaction ε_{DDI},

$$\varepsilon = A_{\text{ex}}(\nabla \boldsymbol{m})^2 + D\boldsymbol{m} \cdot (\nabla \times \boldsymbol{m}) - K(\boldsymbol{m} \cdot \hat{\rho})^2 + E_{\text{DDI}}, \tag{2}$$

where A_{ex} is the exchange stiffness, D is the bulk DMI constant, and K is the uniaxial anisotropy constant along the radial direction $\hat{\rho}$. We adopt material parameters from bulk FeGe[54] to ensure comparability with earlier works and to benchmark the skyrmion behavior in a well-characterized chiral magnetic material. However, nanostructures made of FeGe, such as the wedge-shaped nanostripes,[66] nanodisks,[67,68] and nanowires,[69] have been experimentally fabricated. Our approach is consistent with several prior studies on curvature-induced effects in skyrmions.[6,14] The material parameters are as follows: saturation magnetization $M_{\text{s}} = 1.1 \times 10^5$ A/m, exchange stiffness $A_{\text{ex}} = 8.78 \times 10^{-12}$ J/m, DMI constant $D = (0.8\text{–}1.5) \times 10^{-3}$ J/m^2 and anisotropy $K_\rho = (1.2\text{–}3.0) \times 10^5$ J/m^3. These values yield an exchange length of approximately 33.9 nm. The simulations employed a spatial discretization of $2 \times 2 \times 2$ nm^3, which is smaller than the exchange length, ensuring numerical accuracy.

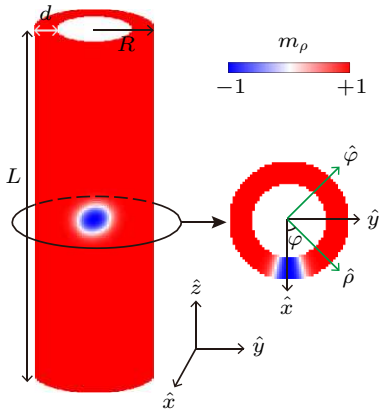


Fig. 1. Diagrammatic representation of a Bloch-type skyrmion stabilized on a magnetic nanotube, where d is the thickness of the tube and R is the outer radius. The origin is at the center of the tube, with $\hat{\rho}$, $\hat{\varphi}$, and $\hat{z}$ representing the radial distance from the magnetic nanotube axis, azimuthal angle, and axial directions, respectively.

To explore skyrmion excitation modes, a sinc-function microwave magnetic field was applied along the $\hat{z}$-direction for 10 ns:

$$\boldsymbol{h}(t) = h_0 \sin[\omega_{\text{c}}(t - t_0)]/[\omega_{\text{c}}(t - t_0)]\hat{z} \tag{3}$$

with $\mu_0 h_0 = 10$ mT, cutoff frequency $\omega_c/2\pi = 100$ GHz, and $t_0 = 1$ ns. This broadband pulse enables excitation of all relevant dynamic modes. For all excitation modes, we used a smaller damping constant of $\alpha = 0.01$ to achieve better spectral resolution, making the data more suitable for analysis. We systematically varied the DMI strength, anisotropy, and nanotube dimensions to construct phase diagrams of skyrmion stability and to characterize the resonant dynamics under external excitation.

3. Results and discussion

Based on the FeGe settings, we numerically compute the phase diagram to determine how a skyrmion can exist in magnetic nanotubes by adjusting the parameters D, K_ρ, and d. The numerical findings are shown in Fig. 2, where three phases are distinguished: saturated state (red color), stable state (blue color), and helical state (green color). When the value of D is small, a saturated state is formed. The phase boundary between the saturated state and the stable state phase is dependent on the mesh size. This is because when D is small, the skyrmion size is also small.[44,55,57] In the case of uniaxial anisotropy K_ρ, it is the opposite [see supplemental material S1]. The detailed analysis is presented as follows.

3.1. Effects of variation in the strength of the bulk DMI and anisotropy K_ρ

It is well known that in planar geometries,[58] the sign of D determines the left or right helicity, while the magnitude of D determines the size of a skyrmion. Thus, we first examined the influence of D on the stability of the skyrmion in the geometry of the magnetic nanotube. The calculations carried out in this instance take into account a set of magnetic parameters and a specific geometry ($L = 600$ nm, $d = 10$–40 nm, inner radius $r = 30$ nm, and outer radius $R = 50$ nm), $K_\rho = 2 \times 10^5$ J/m^3 and a bulk DMI parameter D varying from 0.8×10^{-3} J/m^2 to 1.50×10^{-3} J/m^2 to evaluate the stable states of skyrmions in cylindrical magnetic nanotubes. The results show that skyrmions are more stable for these D values in the interval between 0.96×10^{-3} J/m^2 to 1.36×10^{-3} J/m^2, as shown in Fig. 2(a). Magnetization of the z component is shown in Figs. 2(b)–2(d) for various relaxed states and values D. We observe a saturated state (see Fig. 2(b) for $D = 0.8 \times 10^{-3}$ J/m^2) if the D constant is below the minimum value of the stable state range (Fig. 2(c) shows a stable state for $D = 1.2 \times 10^{-3}$ J/m^2). However, as shown in Fig. 2(d) for $D = 1.4 \times 10^{-3}$ J/m^2, a helical state emerges for $D > 1.36 \times 10^{-3}$ J/m^2. This phenomenon is explained by the competition between anisotropy and DMI, which determines the stable state. In other words, when D is small, the system's primary interaction is uniaxial anisotropy, leading to a lower energy state that minimizes this contribution to the total energy. In contrast, as D increases, the DMI becomes more significant in determining the stable state, resulting in the emergence of the helical state at high D values.

As is well-known, the stabilization of skyrmions in planar films is largely dependent on the confinement effect of the sample border. Similarly, the phase boundary between the stable state phase and the helical state phase depends on the diameter of the tube.[57] For a stable skyrmion state in planar films, the maximum limit of D is greater in a small sample than in an infinite film.[57,58] The reason for the lower limit of D in this magnetic nanotube is likely that the skyrmion size exceeds the magnetic nanotube's diameter, unlike in an infinite film. Due to the demagnetizing field, the skyrmion size increases with diameter, similar to planar geometry.[55,57] The cross-sectional top view cut in the ϕ–z plane (upper) and the front view after unrolling the m_ρ of the magnetic nanotube in a planar ϕ–z plane, where the magnetization component m_z is normalized to zero ($m_z = 0$) to define the skyrmion boundary. We observe that the shape of the skyrmions in the magnetic nanotube is slightly elliptical rather than circular, in contrast to the circular shape of skyrmions created in 2D flat systems like thin films. An ellipse is used to fit the skyrmion's boundary to better define its shape. The semimajor and semiminor axes of the ellipse, represented by d_1 and d_2, respectively, serve as markers for the skyrmion's size and deformation. Figure 3(a) shows the dependence of the stable state skyrmion size on DMI. We notice that the difference between d_1 and d_2 is small when the constant D is small.

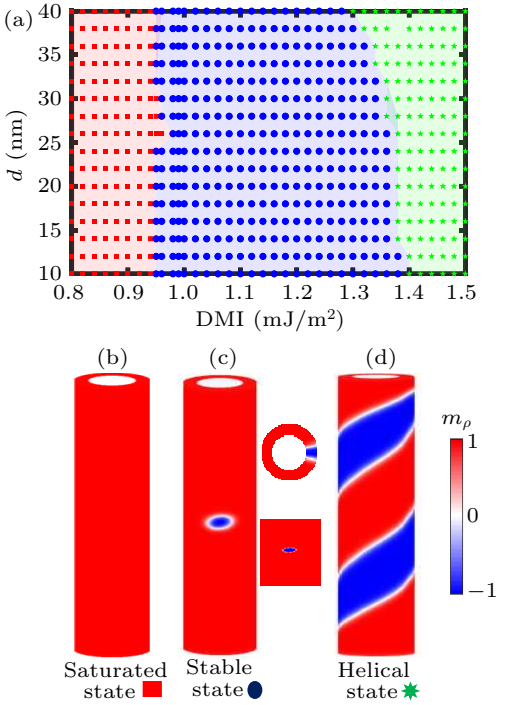


Fig. 2. Magnetic states in magnetic nanotubes. (a) The magnetic phase diagram as a function of D and t. (b) A saturated state. (c) The stability status of the skyrmion. (d) A helicoidal state obtained. The top view and the planar film are at the side of each phase.

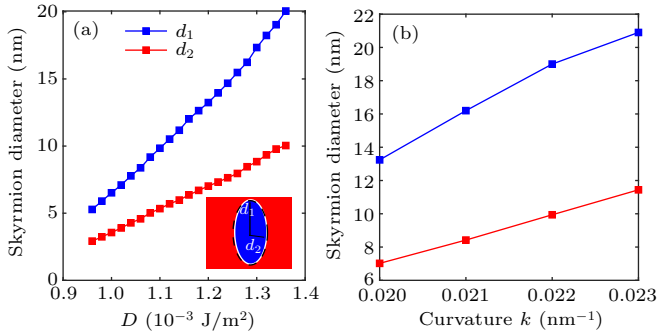


Fig. 3. Skyrmion stability with diameter dependence on (a) DMI constant and (b) curvature. The red and blue colors indicate the skyrmion diameters along the minor and the major axes of the elliptical shape. The skyrmion diameters were estimated to be the size for $m_z = 0$.

For example, in the cylindrical magnetic nanotube with $L = 600$ nm, $d = 20$ nm, inner radius $r = 30$ nm, and outer radius $R = 50$ nm, $K_\rho = 2 \times 10^5$ J/m^3, when $D = 0.96$ mJ/m^2, $d_1 = 2.64$ nm, and $d_2 = 1.46$ nm, the difference $(d_1 - d_2) = 1.18$ nm. However, as the DMI increases to $D = 0.98 \times 10^{-3}$ J/m^2, d_1, d_2, and $d_1 - d_2$ increases to 2.95 nm, 1.62 nm, and 1.33 nm, respectively. When the DMI increases further, d_1 and d_2 also continue to increase. This indicates that larger skyrmions are energetically favorable at higher DMI values. The elliptical shape of skyrmions in curved geometries, such as the magnetic nanotubes studied here, arises from curvature-induced DM-like interactions rather than geometric confinement. We also estimated the values of d_1 and d_2 according to the curvature ($k = 1/R$) with ($L = 600$ nm, $d = 20$ nm, inner radius $r = 30$ nm and outer radius $R = 44$ nm, 46 nm, 48 nm, 50 nm), $K_\rho = 2 \times 10^5$ J/m^3, when $D = 1.2 \times 10^{-3}$ J/m^2 as shown in Fig. 3(b). As the curvature increased, both d_1, d_2, and their difference $(d_1 - d_2)$ for $D = 1.2 \times 10^{-3}$ J/m^2 also increased. For example, when $R = 50$ nm, $d_1 = 6.62$ nm, $d_2 = 3.51$ nm, and the difference $(d_1 - d_2) = 3.11$ nm. As the outer radius decreases to $R = 48$ nm, d_1, d_2, and $d_1 - d_2$ increase to 8.10 nm, 4.21 nm, and 3.89 nm, respectively. Increasing the curvature (decreasing the outer radius of the tube) enforces the stability of the skyrmion formation by increasing its size for D. This clearly shows that the curvature affects the stability of skyrmion formation via a curvature-induced DM-like interaction. To quantify the spatial extent and confinement of skyrmions in different geometries, we estimated the effective skyrmion volume in both planar and nanotube systems. For the planar geometry, we employed the analytical model proposed by Wang *et al.*,[56] which relates the skyrmion radius and wall width to micromagnetic parameters. Using $D = 1.2 \times 10^{-3}$ J/m^2, $A_{ex} = 8.78 \times 10^{-12}$ and $K_\rho = 2 \times 10^5$ J/m^3, the calculated skyrmion radius and wall width are approximately 6.71 nm and 4.71 nm, respectively. The effective skyrmion volume in the planar thin film is estimated as $V_{planar} = \pi R^2 t \approx 666.3$ nm^3.

In contrast, for our nanotube geometry, we used elliptical fitting of the skyrmion cross-section obtained from micromagnetic simulations. The semi-major and semi-minor axes were determined to be $d_1 = 6.62$ nm and $d_2 = 3.50$ nm, respectively, and the wall thickness was $d = 20$ nm. Modeling the skyrmion as an elliptical cylinder, the effective volume is given by $V_{tube} = \pi d_1 d_2 d \approx 1456.0$ nm^3. This comparison shows that skyrmions in nanotubes occupy a larger and more anisotropic volume than in planar films. The increase is attributed to curvature-induced deformation and azimuthal displacement, which are absent in flat systems.

Examining the effects of variations in the anisotropy K_ρ constant on the stability and size of skyrmions in magnetic nanotubes is also fascinating. To determine the range of K_ρ where the magnetic skyrmion exists in a cylindrical magnetic nanotube, we run micromagnetic simulations with magnetic parameters and a specific geometry. The findings indicate that skyrmions stabilize for anisotropy values K_ρ in the range of 165×10^3 J/m^3 to 285×10^3 J/m^3 (detailed can be seen in supplemental material S1). This condition arises because of the high anisotropy value, which encourages the alignment of the magnetic moments in the magnetic nanotube. When the DMI constant is adjusted and the anisotropy value is fixed, the same states are obtained. Stable skyrmions in a nanowire framework can exhibit similar states.[59] We studied the dependence of the stable state skyrmion size and deformation as a function of K_ρ, following the steps in that of the DMI. Figure 4 shows the results of the skyrmion size and deformation as a function of K_ρ. The difference between the values of d_1 and d_2 decreases when K_ρ increases. For example, in a cylindrical magnetic nanotube with $L = 600$ nm, $d = 20$ nm, inner radius $r = 30$ nm, outer radius $R = 50$ nm, and $D = 1.2 \times 10^{-3}$ J/m^2, when $K_\rho = 165 \times 10^3$ J/m^3, $d_1 = 39.68.84$ nm and $d_2 = 18.88$ nm, resulting in a difference of $d_1 - d_2 = 20.80$ nm. However, as K_ρ increases to 170×10^3 J/m^3, d_1, d_2, and $d_1 - d_2$ decrease to 34.56 nm, 16.58 nm and 17.98 nm, respectively. With an increase in K_ρ, both d_1 and d_2 continue to decrease. Increasing the value of K_ρ, forces the magnetic moments to align, thereby reducing the size of the skyrmion. This was also observed in the case of the bimeron in the magnetic nanotube,[61] following an inversely linear function.[57]

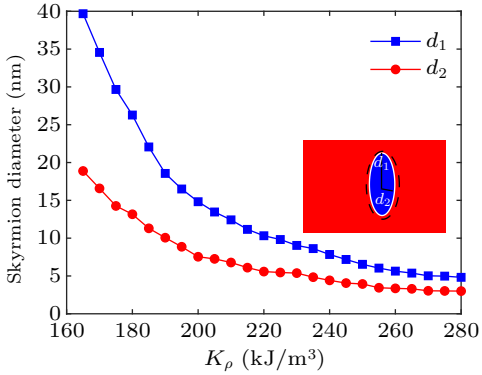


Fig. 4. Skyrmion stability with diameter dependence on K_ρ. The red and blue colors indicate the skyrmion diameters along the minor and major axes of the elliptical shape. The skyrmion diameters were estimated to be the size for $m_z = 0$.

3.2. Mode characteristics and skyrmion dynamics in a magnetic nanotube

By applying a sinc function microwave field $\boldsymbol{h}(t) = h_0 \sin[\omega_c(t-t_0)]/[\omega_c(t-t_0)]\hat{z}$ with $\mu_0 h_0 = 10$ mT, $\omega_c/2\pi = 100$ GHz, and $t_0 = 1$ ns to the skyrmion structure shown in Fig. 1, we were able to analyze the skyrmion mode characteristics. At every 5 ps, the spatiotemporal evolution of the magnetization at each node was recorded while applying the sinc microwave field. Then, to capture all potential modes excited within a frequency range from 0 to 100 GHz, we performed a fast Fourier transform (FFT) on the temporal evolutions of local magnetizations at each node. In the presence of a skyrmion, the spectra (δm_z) show three distinct modes centered at 13.9 GHz, 59.6 GHz, and 75.8 GHz, as seen in Fig. 5(a). The 75.4 GHz mode, which also appears in the absence of a skyrmion, is attributed to the ferromagnetic resonance (FMR) mode, corresponding to the uniform precession of magnetization in the magnetic nanotube as seen in Fig. 5(b). Through this comparison, the ferromagnetic resonant mode is identified at 75.8 GHz. The strong low-frequency peak observed in Fig. 5(a) is attributed to the translational mode of the skyrmion, as reported in previous works.[60] These modes emerge due to the continuous symmetry of the skyrmion structure and are particularly prominent in edge-free or low-confinement geometries such as nanotubes.

In order to differentiate the attributes of the other distinct modes, we applied a microwave field $\boldsymbol{h}(t) = h_0 \sin(\omega_o t)\hat{z}$ with $\mu_0 h_0 = 10$ mT and the corresponding resonance frequency modes. Figure 5(c) shows the temporal variation time for the local distributions of $m_\rho(t)$ and $\Delta m_\rho(t) = [m_\rho(t) - m_\rho(0)]$, where $m_\rho(0)$ is the initial state of m_ρ when time is 0 ns. The temporal variation time of m_ρ, as illustrated in Fig. 5(c), reveals that the modes excited at 13.9 GHz (mode 1) and 59.6 GHz (mode 2) are gyration modes. These modes exhibit CCW rotation, as explicitly illustrated in Fig. 5(c), consistent with the chiral nature of the skyrmion with mode 2 exhibiting a higher frequency compared to mode 1. The frequency splitting between the two gyration modes can be attributed to the radial and azimuthal confinement of the skyrmion within the magnetic nanotube, as well as the interaction between the skyrmion and the magnetic nanotube's curvature.

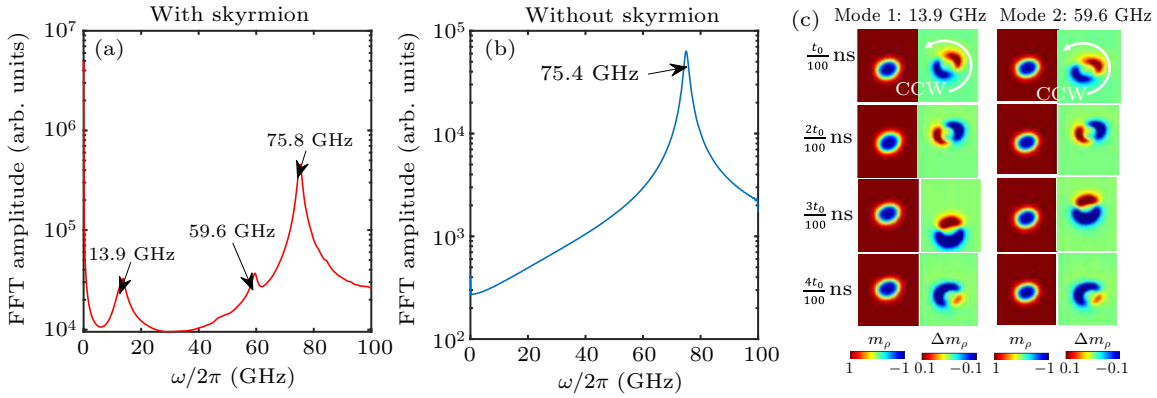


Fig. 5. Fast Fourier transform (FFT) on the temporal evolution of local magnetizations at each node over the entire surface of the magnetic nanotube. (a) With skyrmion. (b) Without skyrmions. (c) Snapshot images of $m_\rho(t)$ and $\Delta m_\rho(t)$, representing the dynamic eigenmodes of the skyrmion, illustrate the CCW gyration modes at 13.9 GHz (mode 1) and 59.6 GHz (mode 2).

The core trajectory of both CCW gyrations exhibits vertical elongation, and this elliptical gyration motion of the skyrmion's core differs from the circular gyration mode that has been reported so far for the skyrmions of 2D planar systems.[62] From the results obtained, we note that the CCW modes are quite distinct from those found in 2D planar geometry. The geometrical asymmetry of the magnetic nanotube (being planar in shape) influences the skyrmion's elliptical and CCW gyration motion. The distinct frequencies and localized nature of these modes highlight their potential for skyrmion-based applications, such as memory devices and magnonic signal processing. This observation is consistent with previous studies, as reported in Ref. [63], where similar gyration dynamics was observed in analogous systems.

To further elucidate the core trajectory and translational motion of a skyrmion in magnetic nanotubes, the m_ρ distribution was unrolled onto the ϕ–z plane, to both the guiding center and the geometric center of the skyrmion core.[64]

The center of the skyrmion is defined by its coordinates (R_ϕ, R_z), which represent the guiding center and the geometric center of the skyrmion core, respectively.[65] These coordinates are calculated as follows:

$$R_\phi = \frac{\int \phi q \, \mathrm{d}\phi \, \mathrm{d}z}{\int q \, \mathrm{d}\phi \, \mathrm{d}z}, \quad R_z = \frac{\int z q \, \mathrm{d}\phi \, \mathrm{d}z}{\int q \, \mathrm{d}\phi \, \mathrm{d}z}, \tag{4}$$

where q is the topological density, expressed as

$$q(\phi, z) = \frac{1}{4\pi} \boldsymbol{m} \cdot \left(\frac{\partial \boldsymbol{m}}{\partial \phi} \times \frac{\partial \boldsymbol{m}}{\partial z} \right). \tag{5}$$

Here, $\boldsymbol{m}$ denotes the magnetization vector.

The snapshots of the spatial distribution m_ρ, illustrating the linear translational motion of the skyrmion core view of

the unrolled magnetic nanotube (detailed can be seen in supplemental material S2). These results were obtained under a magnetic field $h_0 = 150$ mT, a DMI constant $D = 1.2$ mJ/m^2, and an anisotropy constant $K_\rho = 200 \times 10^3$ J/m^3. In both modes, the direction of the core translational motion is along the $-z$-axis. Figures 6(a) and 6(b) show the corresponding core trajectories. Both modes exhibit CCW rotating core gyration motion. The black dot in Figs. 6(a) and 6(b) marks the critical point where the system transitions from a core gyration trajectory to a linear translational motion.

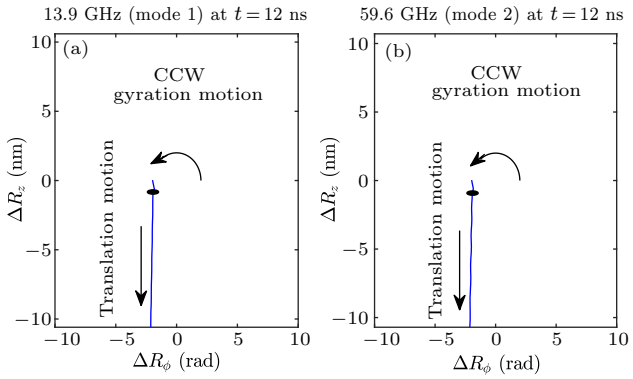


Fig. 6. Core trajectories of the skyrmion of the unrolled magnetic nanotube. (a) The core trajectory at frequency of 13.9 GHz (mode 1). (b) The core trajectory at frequency of 59.6 GHz (mode 2). Both modes exhibit CCW rotating core gyration motion. The black dot marks the critical point where the system transitions from a core gyration trajectory to a linear translational motion.

To further analyze the linear translational motion of the core, we plotted the displacements of the core position (the guiding center of the skyrmion) for both modes, along with the instantaneous velocity v as a function of time, as shown in Fig. 7. The axial (z) displacement R_z (red line) of the core motion exhibits a significant variation over time, indicating pronounced translational dynamics along the magnetic nanotube axis, as shown in Figs. 7(a) and 7(b). In contrast, the azimuthal (ϕ) displacement R_ϕ (blue line) remains nearly constant for most of the observed duration, suggesting minimal rotational motion of the core in the azimuthal direction. However, for Fig. 7(b), a notable change in R_ϕ is observed when the time exceeds 40 ns. This deviation indicates the onset of significant azimuthal motion, likely driven by the interplay between the applied magnetic field, the DMI, and the anisotropy energy at higher excitation frequencies. The transition in R_ϕ behavior underscores the frequency-dependent dynamics of the skyrmion core, where mode 2 (59.6 GHz) induces more complex motion compared to mode 1 (13.9 GHz).

The velocity $\boldsymbol{v} = (v_z, v_\phi)$ of the core motion as a function of time is shown in Figs. 7(c) and 7(d). These plots clearly illustrate the transition point from gyration to linear translational motion. The azimuthal velocity component v_ϕ remains close to zero throughout the time domain, indicating negligible rotational motion.

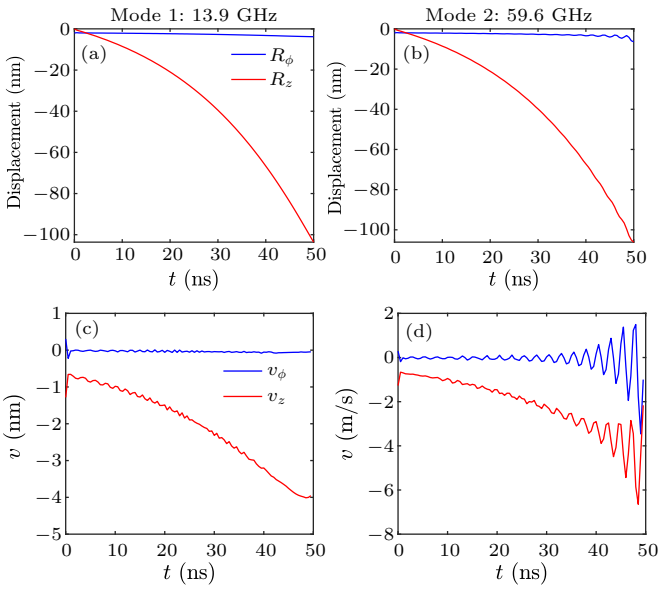


Fig. 7. Displacement and velocity of skyrmion motion according to the guiding center in z (red color) and R_ϕ (blue color). (a) Displacement at 13.9 GHz (mode 1). (b) Displacement at 59.6 GHz (mode 2). (c) Velocity at 13.9 GHz (mode 1). (d) Velocity at 59.6 GHz (mode 2).

In contrast, the axial velocity component v_z initially oscillates around zero but undergoes a sudden change (in the negative direction) at the transition point, as shown in Fig. 7(c). For Fig. 7(d), a similar behavior is observed; however, as the time approaches and exceeds 40 ns, both v_z and v_ϕ exhibit significant changes. This deviation highlights the frequency-dependent dynamics of the skyrmion core, where mode 2 (59.6 GHz) induces more complex motion compared to mode 1 (13.9 GHz). The abrupt changes in v_z and v_ϕ further corroborate the transition from gyration to linear translational motion, emphasizing the role of the applied magnetic field, the DMI and anisotropy energy in governing the core dynamics.

Figure 8 illustrates the effect of the magnetic field h_0 on the average velocity $\bar{\boldsymbol{v}} = (\bar{v}_z, \bar{v}_\phi)$ for mode 1 and mode 2. The magnetic field h_0 was varied from 25 mT to 200 mT to investigate its influence on the skyrmion dynamics. The results reveal different behaviors for the axial and azimuthal velocity components. For the average axial velocity $\bar{v}_z$, Fig. 8(a) shows that it exhibits nonzero values throughout the range of h_0. Specifically, $\bar{v}_z$ ranges from -2.064 m/s to -2.077 m/s for mode 1 and from -2.07 m/s to -2.095 m/s for mode 2, demonstrating a consistent translational motion along the $-z$-axis. This highlights the dominant role of the magnetic field in driving the axial motion of the skyrmion core. As h_0 increased, $\bar{v}_z$ showed a slight but measurable change, indicating enhanced translational motion along the $-z$-axis. This behavior underscores the strong influence of the magnetic field on the skyrmion's translational dynamics.

In contrast, the average azimuthal velocity $\bar{v}_\phi$, shown in Fig. 8(b), remains close to zero for magnetic fields below 125 mT, indicating negligible rotational motion on average. However, above 125 mT, $\bar{v}_\phi$ begins to change significantly,

reaching a value of -0.129 m/s at 200 mT. This suggests that higher magnetic fields induce measurable azimuthal motion, likely due to the interaction between the magnetic field, the DMI, and curvature-induced effects in the magnetic nanotube geometry. These curvature effects arise from the magnetic nanotube geometry, which introduces an effective magnetic field and modifies the spin texture of the skyrion, leading to the observed rotational motion at higher fields. The magnetic field h_0 significantly influences the skyrmion core's velocity components, $\bar{v}_z$ and $\bar{v}_\phi$. As h_0 increases from 25 mT to 200 mT, the following effects are observed: (1) The axial velocity $\bar{v}_z$ represents the translational motion of the skyrmion core along the magnetic nanotube axis (z direction). For mode 1, $\bar{v}_z$ ranges from -2.064 m/s to -2.077 m/s, while for mode 2, it ranges from -2.07 m/s to -2.095 m/s. This indicates a consistent translational motion along the $-z$-axis, driven by the interplay between the magnetic field, DMI, and anisotropy energy. The slight variation in $\bar{v}_z$ with increasing h_0 suggests that higher magnetic fields enhance the translational motion of the skyrmion core. (2) The azimuthal velocity $\bar{v}_\phi$ represents the rotational motion of the skyrmion core around the magnetic nanotube's azimuthal direction (ϕ-direction). At lower magnetic fields ($h_0 < 125$ mT), $\bar{v}_\phi$ remains close to zero, indicating negligible rotational motion. Above 125 mT, $\bar{v}_\phi$ begins to increase significantly, reaching -0.129 m/s at 200 mT. This suggests that higher magnetic fields induce measurable rotational motion, likely due to curvature-induced effects in the magnetic nanotube geometry. (3) The magnetic field also influences the transition from gyration (rotational motion) to linear translational motion. At lower fields, the skyrmion core primarily undergoes gyration, but as h_0 increases, the translational motion becomes more pronounced. This transition is marked by a sudden change in $\bar{v}_z$, as observed in Figs. 8(c) and 8(d), where $\bar{v}_z$ shifts from oscillating around zero to a steady negative value. (4) The direction of the translational motion is influenced by the sign of the DMI constant, as reported by Yang *et al.*[45] In this study, the motion is consistently along the $-z$-axis, which is consistent with the positive sign of the constant DMI in the system. The curvature-induced effects in the magnetic nanotube geometry further modify the skyrmion dynamics, leading to the observed directional changes in translational motion. These effects are distinct from pinning or depinning mechanisms and are intrinsic to the curved geometry of the magnetic nanotube.

A notable feature observed in this study is the dependence of the translational motion direction on the excitation mode and the sign of the DMI constant, as previously reported by Yang *et al.*[45] The direction of the translational motion is influenced by the gyration phase in magnetic nanotubes. This behavior arises from curvature-induced modifications to the skyrmion's spin texture,[45] which generate an effective magnetic field. Unlike in planar systems, these effects are intrinsic to the curved geometry and are distinct from conventional pinning mechanisms.

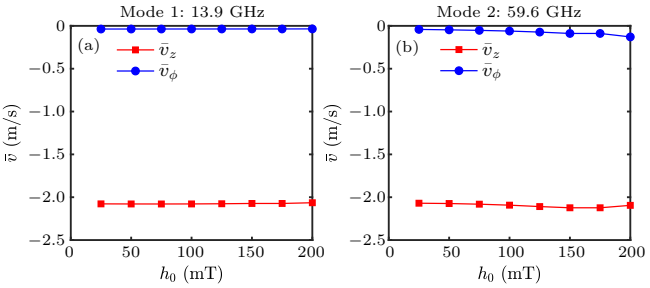


Fig. 8. Effect of magnetic field h_0 on skyrmion average velocity. (a) Frequency of 13.9 GHz (mode 1). (b) Frequency of 59.6 GHz (mode 2).

4. Conclusion

This study has provided a comprehensive exploration of the stability and dynamic behavior of skyrmions in magnetic nanotubes, a geometry that introduces unique curvature effects and cylindrical symmetry. Unlike planar systems, skyrmions in magnetic nanotubes adopt an elliptical shape and are stabilized by the interplay between curvature, the DMI, and the anisotropy constant. Through micromagnetic simulations and numerical modeling, we have mapped out a phase diagram that delineates the stable skyrmion state as a function of varying DMI and anisotropy constants. This phase diagram offers valuable insights into the parameter regimes where skyrmions can be stabilized, while also revealing transitions to other magnetic states, such as saturated and helical configurations, in unstable regions. These findings underscore the complex energy landscape of magnetic nanotubes and the delicate balance required to maintain skyrmion stability.

A key contribution of this work is the identification of distinct dynamic modes of skyrmions, including gyration modes with a CCW rotational sense, which are strongly influenced by the magnetic nanotube's geometric parameters and the applied microwave field. We demonstrated that the magnetic field significantly impacts the skyrmion's velocity components, with the axial velocity $\bar{v}_z$ exhibiting consistent translational motion along the $-z$-axis, while the azimuthal velocity $\bar{v}_\phi$ remains negligible at lower fields but increases significantly at higher fields due to curvature-induced effects. The transition from gyration to linear translational motion, driven by the interplay between the magnetic field, DMI, and curvature effects, further highlights the rich and tunable dynamics of skyrmions in curved geometries. Importantly, the directional changes in motion are not caused by pinning or depinning effects but are instead attributed to curvature-induced additional effects, which modify the skyrmion's spin texture and introduce an effective magnetic field. These results demonstrate that magnetic nanotubes provide a robust platform for hosting skyrmions, with tunable stability and dynamic properties

particularly suited for applications in information processing technologies, such as skyrmion-based memory and logic devices.

Despite these advancements, certain limitations must be acknowledged. The simulations and numerical models employed in this study assume idealized conditions, such as uniform material properties and perfect cylindrical symmetry, which may not fully capture the complexities of real-world systems. Although this study analyzed the gyration dynamics of skyrmions in nanotubes, breathing modes characterized by periodic expansion and contraction of the skyrmion core, remain an important aspect of their dynamic behavior. Additionally, the study does not account for temperature-dependent effects, which could play a significant role in skyrmion stability and motion, particularly in practical applications. Experimental validation is also needed to confirm the predicted behaviors and address potential discrepancies between theoretical models and experimental observations.

Looking ahead, future work should focus on addressing these limitations and expanding the scope of this research. Experimental studies are essential to validate the simulation results and explore the effects of real-world conditions, such as material defects and temperature variations. Investigating temperature-dependent dynamics, particularly in the context of thermal fluctuations and phase transitions, would provide a more comprehensive understanding of skyrmion behavior in practical applications. Investigate breathing mode excitations and compare their properties in curved geometries versus planar systems, where curvature is expected to modify the excitation spectrum due to asymmetry and radial confinement effects. Furthermore, exploring the potential applications of skyrmions in magnetic nanotubes for information processing technologies, such as skyrmion-based racetrack memory, logic gates, and neuromorphic computing, could unlock new avenues for next-generation devices. Extending the study to more complex geometries, such as tapered or helical magnetic nanotubes, and developing multiscale models that combine micromagnetic simulations with atomistic calculations would also provide deeper insights into skyrmion dynamics at different length scales.

In conclusion, this study advances our understanding of skyrmion stability and dynamics in magnetic nanotubes, highlighting the unique role of curvature effects and their potential for technological applications. By addressing the limitations and pursuing the proposed future work, we can further unlock the potential of skyrmions in curved geometries, paving the way for innovative solutions in information processing and beyond.

Acknowledgements

Project supported by the National Key Research and Development Program of China (Grant No. 2022YFA1405900), the National Natural Science Foundation of China (Grant Nos. U2441217 and 12074058), and Sichuan Science and Technology Program (Grant No. 2024YFHZ0372).

References

[1] Fert A and Cros V 2013 *Nat. Nanotechnol.* **8** 152
[2] Zhang X, Zhao G P, Fangohr H, Liu J P, Xia W X, Xia J and Morvan F J 2015 *Sci. Rep.* **5** 7643
[3] Tomasello R, Martinez E, Zivieri R, Torres L, Carpentieri M and Finocchio G 2014 *Sci. Rep.* **4** 6784
[4] Huang Y, Kang W, Zhang X, Zhou Y and Zhao W 2017 *Nanotechnology* **28** 08LT02
[5] Zhang X, Ezawa M and Zhou Y 2015 *Sci. Rep.* **5** 9400
[6] Huo X and Liu Y 2019 *New J. Phys.* **21** 093024
[7] Heinze S, Von Bergmann K, Menzel M, Brede J, Kubetzka A, Wiesendanger R, Bihlmayer G and Blügel S 2011 *Nat. Phys.* **7** 713
[8] Jonietz F, Mühlbauer S, Pfleiderer C, Neubauer A, Münzer W, Bauer A, Adams T, Georgii R, Böni P, Duine R A, *et al.* 2010 *Science* **330** 1648
[9] Yu X Z, Kanazawa N, Zhang W Z, Nagai T, Hara T, Kimoto K, Matsui Y, Onose Y and Tokura Y 2012 *Nat. Commun.* **3** 988
[10] Schulz T, Ritz R, Bauer A, Halder M, Wagner M, Franz C, Pfleiderer C, Everschor K, Garst M and Rosch A 2012 *Nat. Phys.* **8** 301
[11] Iwasaki J, Mochizuki M and Nagaosa N 2013 *Nat. Nanotechnol.* **8** 742
[12] Sampaio J, Cros V, Rohart S, Thiaville A and Fert A 2013 *Nat. Nanotechnol.* **8** 839
[13] Iwasaki J, Mochizuki M and Nagaosa N 2013 *Nat. Commun.* **4** 1463
[14] Abdulrazak T, Liu X, Wang Z, Cao Y and Yan P 2024 *Chin. Phys. B* **33** 107504
[15] Yoo M W, Cros V and Kim J V 2017 *Phys. Rev. B* **95** 184423
[16] Zhang X, Zhou Y and Ezawa M 2016 *Nat. Commun.* **7** 10293
[17] Dzyaloshinsky I 1958 *J. Phys. Chem. Solids* **4** 241
[18] Moriya T 1960 *Phys. Rev.* **120** 91
[19] Mühlbauer S, Binz B, Jonietz F, Pfleiderer C, Rosch A, Neubauer A, Georgii R and Böni P 2009 *Science* **323** 915
[20] Yu X, Kikkawa A, Morikawa D, Shibata K, Tokunaga Y, Taguchi Y and Tokura Y 2015 *Phys. Rev. B* **91** 054411
[21] Jin C M and Du H F 2015 *Chin. Phys. B* **24** 128501
[22] Fert A and Van Dau F N 2019 *C. R. Phys.* **20** 817
[23] Landeros P and Núñez Á S 2010 *J. Appl. Phys.* **108** 034303
[24] Landeros P, Allende S, Escrig J, Salcedo E, Altbir D and Vogel E E 2007 *Appl. Phys. Lett.* **90** 102501
[25] Yan M, Andreas C, Kákay A, García-Sánchez F and Hertel R 2011 *Appl. Phys. Lett.* **99** 122505
[26] Hertel R 2016 *J. Phys.: Condens. Matter* **28** 483002
[27] Bachmann J, Knez M, Barth S, Shen H, Mathur S, Gösele U and Nielsch K 2007 *J. Am. Chem. Soc.* **129** 9554
[28] Weber D P, Rüffer D, Buchter A, Xue F, Russo-Averchi E, Huber R, Berberich P, Arbiol J, Fontcuberta i Morral A, Grundler D, *et al.* 2012 *Nano Lett.* **12** 6139
[29] Buchter A, Nagel J, Rüffer D, Xue F, Weber D P, Kieler O F, Weimann T, Kohlmann J, Zorin A B, Russo-Averchi E, *et al.* 2013 *Phys. Rev. Lett.* **111** 067202
[30] Fernandez-Roldan J A, Chrischon D, Dorneles L S, Chubykalo-Fesenko O, Vazquez M and Bran C 2018 *Nanomaterials* **8** 692
[31] Gaididei Y, Kravchuk V P and Sheka D D 2014 *Phys. Rev. Lett.* **112** 257203
[32] Yershov K, Kravchuk V, Sheka D and Roessler U 2020 *SciPost Phys.* **9** 043
[33] Sheka D D 2021 *Appl. Phys. Lett.* **118** 230502
[34] Kravchuk V P, Rößler U K, Volkov O M, Sheka D D, van den Brink J, Makarov D, Fuchs H, Fangohr H and Gaididei Y 2016 *Phys. Rev. B* **94** 144402
[35] Yang J, Abert C, Suess D and Kim S-K 2021 *Sci. Rep.* **11** 3886

[36] Carvalho-Santos V L, Corona R M, Altbir D and Castillo-Sepúlveda S 2020 *Phys. Rev. B* **102** 024444
[37] Tejo F, Toneto D, Oyarzún S, Hermosilla J, Danna C S, Palma J L, da Silva R B, Dorneles L S and Denardin J C 2020 *ACS Appl. Mater. Interfaces* **12** 53454
[38] Carvalho-Santos V L, Castro M A, Salazar-Aravena D, Laroze D, Corona R M, Allende S and Altbir D 2021 *Appl. Phys. Lett.* **118** 172405
[39] Korniienko A, Kákay A, Sheka D D and Kravchuk V P 2020 *Phys. Rev. B* **102** 014432
[40] Farias W S, Santece I A and Coura P Z 2023 *J. Magn. Magn. Mater.* **568** 170386
[41] Yershov K V, Kákay A and Kravchuk V P 2022 *Phys. Rev. B* **105** 054425
[42] Kechrakos D, Tzannetou L and Patsopoulos A 2020 *Phys. Rev. B* **102** 054439
[43] Yu X and Liu Y 2021 *Phys. Lett. A* **415** 127656
[44] Wang X, Wang X S, Wang C, Yang H, Cao Y and Yan P 2019 *J. Phys. D: Appl. Phys.* **52** 225001
[45] Yang J, Kim J, Abert C, Suess D and Kim S K 2020 *Phys. Rev. B* **102** 094439
[46] Ga Y, Cui Q, Liang J, Yu D, Zhu Y, Wang L and Yang H 2022 *Phys. Rev. B* **106** 054426
[47] Jiang J, Ga Y, Li P, Cui Q, Wang L, Yu D, Liang J and Yang H 2024 *Phys. Rev. B* **109** 014402
[48] Müller J and Rosch A 2015 *Phys. Rev. B* **91** 054410
[49] Zhang X, Zhou Y and Ezawa M 2016 *Sci. Rep.* **6** 24795
[50] Dupé B, Hoffmann M, Paillard C and Heinze S 2014 *Nat. Commun.* **5** 4030
[51] von Malottki S, Dupé B, Bessarab P F, Delin A and Heinze S 2017 *Sci. Rep.* **7** 12299
[52] Hagemeister J, Romming N, Von Bergmann K, Vedmedenko E Y and Wiesendanger R 2015 *Nat. Commun.* **6** 8455
[53] Vansteenkiste A, Leliaert J, Dvornik M, Helsen M, Garcia-Sanchez F and Van Waeyenberge B 2014 *AIP Adv.* **4** 107133
[54] Wang W, Albert M, Beg M, Bisotti M A, Chernyshenko D, Cortès-Ortuño D, Hawke I and Fangohr H 2015 *Phys. Rev. Lett.* **114** 087203
[55] Büttner F, Lemesh I and Beach G S D 2018 *Sci. Rep.* **8** 4464
[56] Wang X S, Yuan H Y and Wang X R 2018 *Commun. Phys.* **1** 1
[57] Wang X S, Yuan H Y and Wang X R 2018 *Commun. Phys.* **1** 31
[58] Rohart S and Thiaville A 2013 *Phys. Rev. B* **88** 184422
[59] Yoo J W, Lee S J, Moon J H and Lee K J 2014 *IEEE Trans. Magn.* **50** 2500404
[60] Mochizuki M 2012 *Phys. Rev. Lett.* **108** 017601
[61] Galvez D, Castro M, Bittencourt G, Carvalho V and Allende S 2023 *Nanomaterials* **13** 2841
[62] Mochizuki M 2012 *Phys. Rev. Lett.* **108** 017601
[63] Abdulrazak T, Liu X, Jin Z, Cao Y and Yan P 2024 *Chin. Phys. B* **33** 087503
[64] Papanicolaou N and Tomaras T N 1991 *Nucl. Phys. B* **360** 425
[65] Abdulrazak T, Liu X, Wang Z, Cao Y and Yan P 2024 *Chin. Phys. B* **33** 107504
[66] Jin C, Li Z A, Kovács A, Caron J, Zheng F, Rybakov F N, Kiselev N S, Du H, Blügel S, Tian M and Zhang Y 2017 *Nat. Commun* **8** 15569
[67] Zheng F, Li H, Wang S, Song D, Jin C, Wei W, Kovács A, Zang J, Tian M, Zhang Y and Du H 2017 *Phys. Rev. Lett* **119** 197205
[68] Zhao X, Jin C, Wang C, Du H, Zang J, Tian M, Che R and Zhang Y 2016 *Proc. Natl. Acad. Sci. USA* **113** 4918
[69] Stolt M J, Li Z A, Phillips B, Song D, Mathur N, Dunin-Borkowski R E and Jin S 2017 *Nano Lett.* **17** 508